Research Square

Preprints are preliminary reports that have not undergone peer review.
They should not be considered conclusive, used to inform clinical practice,
or referenced by the media as validated information.

Volumetric Bioprinting of Aqueous Two-Phase Emulsion Bioinks Enables High-Fidelity Macroporous Hydrogel Scaffolds for Volumetric Muscle Loss Repair

Guosheng Tang

guoshengtang@gzhmu.edu.cn

Guangzhou Medical University https://orcid.org/0009-0009-2791-8448

yingying hou

5. The Fourth Affiliated Hospital of Guangzhou Medical University; School of Biomedical Engineering, Guangzhou Medical University, Guangzhou 511436, P. R. China

Long Chen

Guangzhou Medical University

Jieting Li

Guangzhou Medical University

Ting Xie

Guangzhou Medical University

Yongrui Cai

Orthopedic Research Institute, Department of Orthopedics, West China Hospital, Sichuan University

Boyi Jiang

Sichuan University

Wenqi Xiao

Guangzhou Medical University

Yahao Lai

West China Hospital, Sichuan University

Leyan Xuan

Junfang Shi

LONGTIME Biopharmaceutical Co., Ltd.

Jinpeng Chen

Guangzhou Medical University

Di Wu

Shanghai Sixth People's Hospital Affiliated to Shanghai Jiao Tong University School of Medicine

Xiaolan Mo

Guangzhou Womenand Children's Medical Center, Guangzhou Medical University

Xin Li
Guangzhou Medical University
Zeyu Luo
West China Hospital, Sichuan University https://orcid.org/0009-0003-3890-0784
Maobin Xie
Harvard Medical School https://orcid.org/0000-0001-9082-4510

Article

Keywords: Volumetric bioprinting, Aqueous two-phase emulsion bioink, Porous hydrogel, Volumetric muscle loss, Muscle regeneration, Regenerative medicine

Posted Date: June 9th, 2026

DOI: https://doi.org/10.21203/rs.3.rs-9948396/v1

License: This work is licensed under a Creative Commons Attribution 4.0 International License.
Read Full License

Additional Declarations: There is **NO** Competing Interest.

Abstract

3D bioprinting holds great promise for tissue engineering by enabling the fabrication of tissue-mimetic, cell-laden constructs. However, traditional bulk hydrogels are restricted by dense nanoscale networks, which impede nutrient diffusion, cell viability, and migration, thus compromising regenerative efficacy. Although emerging aqueous two-phase emulsion bioinks permit the generation of favorable macroporous architectures, such systems suffer from intrinsic instability during room-temperature storage or under mechanical stimuli (e.g., extrusion or digital light processing). This instability leads to phase segregation, which disturbs micropore formation and severely narrows the operational time window for reliable bioprinting. Here, we propose a strategy utilizing volumetric bioprinting (VBP) to process aqueous two-phase emulsion bioinks. Benefiting from VBP's ultrafast in situ fabrication via dynamic photopolymerization under full-volume illumination, this approach effectively suppresses phase segregation while improving the stability and printability of the bioinks. Using a volumetric muscle loss (VML) repair model, we demonstrate that the porous hydrogel constructs laden with adipose-derived mesenchymal stem cells (MSCs) exhibit significantly enhanced therapeutic efficacy compared with conventional bulk hydrogels. Our findings highlight that volumetric bioprinting of aqueous two-phase emulsion bioinks represents a versatile platform for fabricating stable porous hydrogels, which may advance the development and translation of porous hydrogel systems in regenerative medicine.

1. Introduction

3D bioprinting has emerged as a transformative technology in regenerative medicine, enabling the precise fabrication of cell-laden constructs that recapitulate key features of native tissue architecture [1–3]. Through layer-by-layer deposition of bioinks, this technique allows the controlled spatial organization of cells and biomaterials, thus facilitating the creation of complex and functional tissue analogs [4–6]. These advances offer substantial promise for diverse applications including organ regeneration, drug screening, and personalized medicine [7]. However, conventional bulk hydrogels—widely employed as bioinks—suffer from inherent limitations imposed by their dense nanoscale polymer networks. Such tightly crosslinked structures impede efficient nutrient and oxygen diffusion, giving rise to hypoxic microenvironments that compromise cell viability and metabolic activity [8]. Moreover, the small pore size restricts cell migration, proliferation, and cell–cell communication, ultimately limiting extracellular matrix remodeling and tissue maturation [9]. As a result, the regenerative potential of bioprinted constructs is often compromised, leading to suboptimal functionality and poor integration after implantation. To address these challenges, macroporous hydrogel scaffolds have attracted growing attention, owing to their superior mass transport, enhanced cell–cell interactions, and ability to support tissue ingrowth [10–12]. Numerous strategies have been developed for the fabrication of porous scaffolds, including porogen leaching [13, 14], microgel annealing [15, 16], and aqueous two-phase emulsion techniques [17, 18].

Aqueous two-phase emulsion (ATPE) represents a facile and effective approach to produce soft, cytocompatible, and hierarchically porous scaffolds suitable for biological systems containing living

cells or bioactive molecules [19–21]. Although ATPE-based bioinks enable the formation of macroporous architectures that overcome diffusion limitations in conventional bulk hydrogels, their practical application is severely hindered by intrinsic instability under typical processing conditions. This instability leads to phase segregation during prolonged storage at ambient temperature or under mechanical forces encountered during extrusion bioprinting or digital light processing (DLP), which disturbs micropore uniformity and drastically narrows the reliable processing window. Volumetric bioprinting (VBP) addresses these challenges by enabling single-exposure, whole-object fabrication. This technique projects dynamically evolving light patterns into specific volumetric regions of bioink within a transparent vial, while synchronously rotating the vial perpendicular to the incident light axis [22, 23]. Photocrosslinking occurs selectively in volumes where accumulated light exposure exceeds the threshold dose, enabling rapid solidification with high shape fidelity [24]. In contrast to traditional layer-by-layer bioprinting, VBP allows ultra-rapid, contactless, and perturbation-free in situ fabrication [25, 26]. This method not only accelerates the production of complex 3D geometries but also eliminates mechanical disturbances during printing, making VBP a powerful platform for the precise manufacturing of macroporous hydrogel constructs [27].

Volumetric muscle loss (VML) is a severe musculoskeletal injury characterized by the irreversible loss of large skeletal muscle volume, which exceeds the body's innate regenerative capacity and leads to chronic functional impairment, fibrotic scarring, and diminished contractile performance [28–30]. Despite the exploration of surgical interventions such as autologous muscle transfer and acellular scaffold implantation [31], clinical outcomes remain unsatisfactory. Inadequate vascularization and limited host cell infiltration often result in incomplete tissue remodeling and a scar-dominated microenvironment. Meanwhile, insufficient control over scaffold microarchitecture and mechanical properties further impairs integration with the surrounding native muscle tissue [32]. These challenges underscore an urgent demand for advanced biomaterials and biofabrication strategies that can generate defect-matching constructs with interconnected porous networks to facilitate cell migration, nutrient diffusion, vascular invasion, and structured muscle regeneration.

Here, we present a robust strategy that combines VBP with ATPE bioinks (**Schematic 1**). By capitalizing on the ultra-rapid in situ photopolymerization enabled by full-volume light exposure, VBP rapidly stabilizes the emulsion structure and mitigates phase segregation, thereby improving bioink stability and broadening the reliable processing window for 3D bioprinting. In contrast to conventional extrusion- or DLP-based printing, the contactless and perturbation-free nature of VBP effectively preserves the internal microstructure of ATPE bioinks, enabling the reproducible fabrication of macroporous hydrogels with tunable architectures. These well-defined porous hydrogels enhance mass transport, support host cell infiltration, and promote the survival and proliferation of encapsulated cells—all critical for effective skeletal muscle regeneration. Using a rat VML injury model, we demonstrate that VBP-printed porous hydrogel constructs, especially when combined with adipose-derived mesenchymal stem cells (MSCs), significantly enhance tissue remodeling and functional recovery compared with conventional bulk hydrogels. Collectively, our work establishes VBP of ATPE bioinks as a versatile and promising platform

for the design and manufacture of defect-matching macroporous hydrogel scaffolds toward skeletal muscle tissue engineering and VML repair.

Schematic 1. Volumetric bioprinting (VBP) of aqueous two-phase emulsion (ATPE) bioinks to fabricate cell-laden macroporous hydrogels for muscle regeneration. a) By choosing appropriate compositions in the two-phase region, different sacrificial phases (PVA, F127, Dextran) and gel-forming phases (Gelatin, SF, PEGDA) are combined and vortexed to generate ATPE bioinks. b) Comparison of printing strategies for ATPE-based bioinks. (i) Conventional extrusion and DLP printing subject the emulsion to mechanical extrusion or light-induced perturbation, leading to pore deformation and non-uniform micropore structures. (ii) The proposed VBP strategy uses green-light volumetric curing to achieve perturbation-free in situ printing, preserving the emulsion architecture and producing scaffolds with uniform microporosity. c) Conceptual illustration of ATPE-VBP hydrogels for VML therapy.

2. Results

2.1 High-Resolution Fabrication of Controllable Macroporous Hydrogels Based on ATPE Bioinks

The fabrication of macroporous hydrogel scaffolds with well-defined, tunable architectures is of central importance for tissue engineering, as such structures markedly improve mass transport, cell infiltration, and integration with host tissues. While ATPE systems have emerged as an effective strategy to generate interconnected porous matrices, their practical implementation is severely hampered by intrinsic physical instability. In particular, shear forces imposed during conventional extrusion-based bioprinting readily induce undesirable phase separation, compromising the uniformity and integrity of the resulting pore networks. To overcome this critical limitation, we hypothesized that the integration of ATPE bioinks with VBP would enable rapid, non-perturbative solidification and thereby stabilize the emulsion structure during printing, allowing the reliable formation of uniform macroporous hydrogel constructs.To test this hypothesis, we first developed an ATPE bioink composed of poly(vinyl alcohol) (PVA) as the sacrificial phase and gelatin as the gel-forming matrix. Guided by previous reports demonstrating that emulsion composition dictates porous morphology, we systematically varied the volumetric ratio of PVA to gelatin from 1:19 to 1:1 to tune the internal pore structure. With increasing PVA content, the emulsions exhibited progressively enlarged dispersed domains, leading to increasingly distinct and expanded macroporous structures (Fig. 1a). As shown in Fig. 1b, we observed a clear transition from sparsely distributed cavities at low sacrificial phase ratios (1:19) to densely packed, interconnected porous networks at higher ratios (1:1). The mean pore diameter increased from approximately 20 μm in low-PVA formulations to over 150 μm in high-PVA groups (Fig. 1c). Correspondingly, total porosity rose from below 5% to above 50% (Fig. 1d)..

Despite the ability to precisely tailor pore size and porosity via simple compositional adjustments, stabilizing ATPE bioinks during printing remained a major technical challenge due to their inherent susceptibility to shear- and time-dependent phase separation. Here, we exploited VBP to rapidly stabilize

and pattern the emulsion bioinks through full-volume photopolymerization. In contrast to traditional layer-by-layer deposition, VBP enables non-contact, interference-free, and ultrafast fabrication by projecting dynamic light patterns through the entire volume of the bioink within a rotating vessel (Fig. 1e). Gelatin and PVA were premixed with photoinitiators, and the emulsion was then exposed to spatially modulated light, allowing the entire 3D construct to be solidified within tens of seconds. This in situ, undisturbed fabrication mode effectively prevents phase separation and preserves the emulsion microstructure prior to destabilization, thus maintaining the spatial uniformity of the nascent pore network.

Notably, the light-scattering nature of ATPE bioinks could potentially introduce optical challenges during VBP. Specifically, the presence of emulsion droplets imparts slight turbidity, which may increase light scattering and refraction during projection, thereby distorting light delivery and compromising printing resolution. To evaluate whether such optical interference impairs spatial fidelity, we designed a CAD model with alternating positive and negative features and printed it using both pure gelatin and gelatin–PVA emulsion bioinks. As shown in Fig. 1f, the incorporation of the sacrificial phase did not noticeably compromise printing resolution or structural accuracy. Constructs from both pure gelatin and gelatin–PVA formulations faithfully reproduced the designed geometries with feature deviations below approximately 30 μm, confirming the compatibility of ATPE bioinks with VBP. Encouraged by these results, we further demonstrated the versatility of this approach by fabricating complex architectures including a threaded screw, rabbit, dinosaur, and human ear (Fig. 1g–j, **Figure S1**). All constructs maintained high morphological fidelity, with well-resolved contours and surface features, and exhibited no macroscopic distortion or collapse (**Figure S2**). These results establish that the combination of ATPE systems with VBP provides a robust platform for generating macroporous scaffolds with tunable architecture and excellent structural fidelity, thereby expanding their applicability in regenerative medicine.

2.2 Comparison of Forming Effects and Internal Macroporous Structures of Different Printing Strategies

After confirming that VBP enables stable processing of ATPE bioinks without sacrificing resolution or geometric fidelity, we next systematically compared VBP with widely used conventional biofabrication techniques—extrusion and digital light processing (DLP) printing—to evaluate their ability to preserve structural uniformity and microporosity when processing these physically unstable emulsions.

Given the critical role of pore morphology and spatial homogeneity in tissue-engineered scaffolds, and the distinct working principles of extrusion, DLP, and VBP, we hypothesized that the different printing mechanisms would differentially influence the structural uniformity and final porous architecture of the printed constructs. We prepared gelatin–PVA ATPE bioinks and printed standardized CAD models (spheroid, screw, nose) using each technique (Fig. 2a). As shown in Fig. 2b, constructs fabricated by extrusion printing displayed irregular surfaces, significant macroscopic deformation, and poor retention of geometric detail, likely due to shear stresses and mechanical disturbances inherent to the extrusion

process. In comparison, DLP printing of ATPE bioinks resulted in incomplete or unstable constructs (Fig. 2c). The layer-by-layer vat polymerization process requires continuous structural support during the peel step, making reliable fabrication of models with small contact areas difficult. Furthermore, the repeated vertical motion and peeling forces perturb the emulsion and accelerate phase separation. In striking contrast, VBP-printed constructs faithfully replicated all designed geometries, with smooth surfaces and precise reproduction of fine features (Fig. 2d). These observations clearly demonstrate that VBP offers distinct advantages for processing physically unstable emulsion bioinks, enabling robust and accurate patterning without compromising structural fidelity.

To further elucidate how each printing method affects internal microporosity, we examined pore morphology and spatial uniformity across the height of printed constructs (Fig. 2e). Consistent with our hypothesis, scaffolds produced by different printing strategies exhibited drastically different internal microstructures. Extrusion-printed constructs showed anisotropic, compressed voids with local collapse, and pores were elongated along the deposition direction (Fig. 2e-i). This behavior is consistent with high shear and compressive forces during extrusion and layer stacking, which deform emulsion droplets, promote coalescence at filament junctions, and partially collapse pores during layer deposition. In contrast, DLP-printed constructs displayed pronounced vertical heterogeneity in pore structure (Fig. 2e-**ii**). Pores near the top surface were relatively small and uniform, while larger, coarsened features and discontinuous channels appeared toward the bottom. This height-dependent gradient can be attributed to the prolonged residence time of the bioink in the vat during layer-by-layer fabrication, combined with mechanical perturbations from repeated peeling, both of which accelerate phase separation and droplet coarsening in lower layers. As expected, VBP-printed constructs maintained spatially uniform, near-spherical pores throughout the entire volume (Fig. 2e-**iii**). The brief full-volume exposure simultaneously arrests phase separation across the entire construct, and the non-contact operation minimizes hydrodynamic stress. Consequently, pore size and distribution remain consistent throughout the scaffold height, preserving a uniform porous network. Quantitative analysis of pore size and porosity confirmed these observations, revealing consistently high and spatially uniform porosity in VBP samples compared to the severe heterogeneity in DLP and structural distortion in extrusion-printed constructs. Collectively, these findings highlight the clear superiority of VBP in preserving geometric fidelity, structural integrity, and uniform microporosity when processing ATPE bioinks.

2.3 Effects of Different ATPE Bioinks Combinations on Microstructure Regulation and Mechanical Properties

Having demonstrated the stable, high-fidelity printing of ATPE bioinks via VBP, we next sought to establish the generality of this strategy by exploring a series of material combinations with distinct physicochemical and biological properties. Our goal was to confirm that the tunable porous structures achieved in the PVA–gelatin system could be generalized across diverse sacrificial and gel-forming phases, thereby broadening the applicability of these macroporous hydrogel scaffolds. We systematically evaluated multiple aqueous two-phase systems by varying the sacrificial phase (PVA,

Pluronic F127, dextran) and the gel-forming phase (gelatin, silk fibroin (SF), polyethylene glycol diacrylate (PEGDA)) (Fig. 3a), investigating how these combinations influence porous microarchitecture, printing fidelity, and mechanical performance.We first varied the sacrificial phase while keeping the gel matrix constant. In addition to PVA, both F127 and dextran formed stable ATPE bioinks with gelatin (**Figure S3**). As shown in Fig. 3b, F127/gelatin scaffolds produced large, uniformly distributed, near-spherical pores. By comparison, dextran/gelatin formulations generated smaller, more densely packed pores with relatively lower spatial homogeneity. These differences can be rationalized by variations in phase viscosity and interfacial properties: higher viscosity in the dispersed phase tends to produce larger, more stable droplets, while lower viscosity favors smaller droplets under equivalent shear. The high viscosity of the F127-rich phase likely limited droplet breakup and promoted mild coalescence, templating larger pores. In contrast, dextran remained sufficiently fluid to form a stable water-in-water emulsion with gelatin, favoring smaller and more numerous droplets. We further expanded the versatility of this platform by employing alternative gel-forming phases (Fig. 3c). Both SF (natural polymer) and PEGDA (synthetic polymer) yielded robust porous structures, yet with distinct microarchitectures. PVA/SF scaffolds exhibited a uniform, fine-pored network, while dextran/PEGDA scaffolds contained larger pores with a broader size distribution. Overall, all material combinations yielded well-defined porous networks, confirming the robustness of the ATPE-templating strategy across diverse polymer systems. Differences in emulsion droplet size and spatial distribution were primarily governed by polymer concentration, solution viscosity, and interfacial tension, which control the capillary number and droplet breakup/coarsening kinetics during emulsification. Quantitative analysis of pore size and porosity confirmed material-dependent differences across formulations (Fig. 3d,e). As expected, the microporous structure in each system could still be tuned by adjusting the volumetric ratio between the two phases.

To verify that complex 3D geometries could be reliably printed across these diverse ATPE formulations, we fabricated challenging architectures including spheres, cartoon cats, teeth, bowls, and helical hollow cylinders. As shown in Fig. 3f, g and **Figure S4**, all ATPE combinations reproduced the target geometries with high accuracy, even for delicate hollow channel constructs. These results confirm that VBP can accommodate the diverse emulsion and rheological characteristics of different ATPE bioinks when paired with optimized printing parameters.

We next investigated how ATPE composition influences the bulk mechanical behavior of printed scaffolds (Fig. 3h). Uniaxial compression testing revealed that all groups exhibited a typical J-shaped stress–strain curve with an initially low modulus and pronounced strain stiffening at elevated strains, characteristic of soft porous hydrogels (Fig. 3i, j). When varying only the sacrificial phase while maintaining gelatin as the matrix, F127/gelatin constructs sustained the highest stresses at a given strain, PVA/gelatin showed intermediate behavior, and dextran/gelatin scaffolds were the most compliant (Fig. 3i). This trend was mirrored in the Young's modulus: F127-based scaffolds displayed the highest stiffness, followed by dextran and then PVA (Fig. 3k). Changing the gel-forming phase had an even more pronounced effect on mechanical properties. Replacing gelatin or SF with PEGDA dramatically increased mechanical strength; dextran/PEGDA constructs reached near-limiting stresses in the measurement window and exhibited a modulus nearly an order of magnitude higher than

protein-based hydrogels (Fig. 3j). These results indicate that both the sacrificial phase and—more significantly—the gel-forming phase provide powerful handles for tuning scaffold stiffness, allowing ATPE bioinks to span a wide range from soft, deformable matrices to reinforced, load-bearing constructs. For comparison, we also evaluated the corresponding bulk gels without the sacrificial phase (**Figure S5**). The relative stiffness ranking of pure gels matched that of porous constructs. PEGDA gels exhibited a steep stress–strain curve and a modulus in the MPa range, whereas gelatin and SF gels remained in the tens of kPa range, with SF slightly stiffer than gelatin. Although introducing the sacrificial phase reduced the absolute modulus, the intrinsic material dependence was preserved, confirming that the mechanical profile of ATPE-derived scaffolds is primarily dictated by the continuous gel network chemistry, with the sacrificial phase providing secondary but tunable control over stiffness. We further characterized the degradation profiles of different ATPE-derived scaffolds (**Figure S6**). In PBS at 37°C, all gelatin- and PEGDA-based emulsion-templated hydrogels underwent rapid mass loss and were nearly fully degraded within 6–8 days. In contrast, SF/PVA hydrogels exhibited markedly prolonged degradation, retaining over 80% of their initial mass after 10 days and eroding completely only after approximately four weeks. Together, these findings demonstrate that ATPE bioinks enable the coordinated tuning of pore architecture, mechanical stiffness, and degradation kinetics, providing a flexible platform to match scaffold properties to the specific requirements of muscle and skin tissue regeneration.

2.4 Evaluation of Cell Viability, Proliferation, and Morphology of ATPE Bioinks

We next validated whether VBP-printed ma

croporous scaffolds effectively support cellular viability, proliferation, and function—essential criteria for advanced tissue engineering applications. We hypothesized that the uniform microporosity of VBP-fabricated hydrogels would significantly enhance cell infiltration, nutrient diffusion, and biological performance compared to conventional non-porous scaffolds.To test this, we encapsulated 3T3 fibroblasts and H9c2 rat cardiomyocytes within gelatin/PVA ATPE bioinks and used VBP to fabricate customized porous scaffolds (Fig. 4a, d). Both cell types exhibited excellent post-printing viability. Live/Dead staining showed predominantly green fluorescent live cells with negligible red dead cells over 7 days of culture (Fig. 4b, e, **Figure S7**). Quantitatively, cell viability remained above 95% at all time points, indicating no cytotoxic effects from the ATPE bioink or printing process (Fig. 4c,f). In parallel, cells maintained normal morphology and distribution within the porous hydrogel scaffolds, suggesting that the PVA–gelatin matrix provides a cytocompatible 3D microenvironment. Importantly, no marked differences in viability were observed between 3T3 and H9c2 cells, underscoring the broad cytocompatibility of this bioink for both connective-tissue and muscle-derived cells. Beyond survival, encapsulated cells proliferated robustly over the culture period. Metabolic activity assays revealed a steady increase in cell number/metabolism, with OD values rising significantly from day 1 to day 7. By day 7, both 3T3 and H9c2 constructs showed approximately 2–3-fold higher OD readings compared to

day 1 (Fig. 4c, f), indicating substantial cell growth within the scaffolds. This consistent proliferative activity, paired with persistently high viability, demonstrates that the PVA–gelatin ATPE bioink supports not only cell survival but also active cell division and expansion.Adequate vascularization is indispensable for the survival and integration of engineered tissues, and scaffold microarchitecture—particularly pore size—regulates endothelial organization into functional, perfusable networks. In volumetric muscle loss (VML) and skin injury repair, rapid vascularization is critical to sustain transplanted cells, accelerate graft integration, and prevent ischemic necrosis. To assess whether printed constructs support this process, HUVECs were cultured on PVA/gelatin scaffolds with four pore conditions: non-porous, ~ 15 μm, ~ 60 μm, and ~ 120 μm (Fig. 4g, **Figure S8**). On day 1, cells in all groups adhered but remained mostly rounded with limited spreading. By day 4, pore-dependent differences emerged. Porous scaffolds, most notably the ~ 120 μm condition, promoted early elongation and cell–cell contact, whereas cells in non-porous gels remained isolated and spherical. By day 7, the ~ 120 μm scaffolds supported short multicellular cords and nascent network formation, in contrast to the scattered distribution observed in non-porous gels. The ~ 60 μm pores allowed bridging between adjacent cavities but produced compact clusters constrained by limited space. By day 14, pore-size-dependent differences in HUVEC organization became fully pronounced. The ~ 120 μm porous scaffolds supported extensive capillary-like network formation, with markedly elongated and interconnected HUVECs forming lumen-like multicellular structures spanning across pores. In the ~ 60 μm pore scaffolds, HUVECs achieved substantial spreading and formed larger but less frequent multicellular assemblies, tending to line pore surfaces and create thick cord-like arrangements with incomplete bridging. In contrast, non-porous and ~ 15 μm pore scaffolds showed minimal network development even after 14 days; HUVECs remained mostly at the periphery or within isolated microdomains, unable to penetrate and form continuous endothelial networks in the dense hydrogel. These findings confirm that well-designed porous architectures enhance cell infiltration and function: scaffolds with large internal micropores support higher cell viability and activity compared to solid constructs, likely by improving oxygen/nutrient transport and providing contact guidance for cell organization.

2.5 Evaluation of MSCs Biologic Behavior in Different Pore Size Scaffolds

Leveraging the favorable cytocompatibility demonstrated in the preceding sections, we next examined whether this platform supports the stem-cell functions required for effective VML and skin injury repair. Adipose-derived mesenchymal stem cells (MSCs) are highly attractive for these applications due to their multipotent differentiation capacity and potent paracrine pro-angiogenic and immunomodulatory effects. However, translating these benefits into functional grafts requires a supportive three-dimensional niche. Since microarchitecture—particularly pore size—modulates cell survival, expansion, and assembly, we hypothesized that different pore sizes would differentially regulate MSCs viability, proliferation, and cytoskeletal organization.

To investigate this, we fabricated ring-shaped scaffolds from PVA/gelatin ATPE bioinks encapsulated with MSCs to validate whether macroporous scaffolds support stem-cell viability and proliferation (Fig. 5a). As shown in Fig. 5b and **Figure S9**, constructs maintained their geometry during culture, and Live/Dead staining at days 1, 4, and 7 showed that nearly all MSCs remained viable (> 95% live cells) with negligible cell death (Fig. 5c). Metabolic assays confirmed continuous proliferation, with optical density increasing significantly from day 1 to day 7 (Fig. 5d). Notably, metabolic activity approximately doubled between day 4 and day 7 across all groups, amounting to an overall ~ 3–4-fold increase from day 1. These results demonstrate that the PVA/gelatin ATPE bioink provides a highly cytocompatible environment for MSCs, consistent with the ability of porous scaffolds to facilitate nutrient diffusion and cell migration.

We next examined how pore size influences MSCs morphology and network formation over two weeks. MSCs distribution evolved dramatically over time, with pore size strongly governing cell alignment and assembly (Fig. 5e, **Figure S10**). In small-pore (~ 15 μm) scaffolds, cells remained largely rounded on days 1 and 4, with only gradual spreading observed by day 7. Even after 14 days, cells formed only dense clusters with limited alignment. In contrast, MSCs within the ~ 60 μm and ~ 120 μm pore scaffolds rapidly adopted an elongated, spindle-like morphology. Within 4 days, these cells had spread across adjacent pores. This trend intensified by day 7, with cells establishing early cell–cell connections. By day 14, the influence of pore architecture was striking: scaffolds with ~ 120 μm pores supported extensive multicellular networks, with MSCs forming aligned, interconnected strands spanning large voids. These observations indicate that intermediate-to-large pore sizes promote cell migration and the development of aligned cytoskeletal structures, whereas overly small pores physically constrain cells and hinder network assembly.

2.6 Porous MSCs-laden gel enabled muscle regeneration after VML in rat models

We next assessed whether porous hydrogel scaffolds support constructive muscle remodeling in vivo using a rat tibialis anterior (TA) volumetric muscle loss (VML) model. A cylindrical full-thickness defect (5 mm diameter × 5 mm height) was created and treated with: MSCs only (MSCs), non-porous gel (NP-G), porous gel (P-G), or porous gel loaded with MSCs (P-G-MSCs). Untreated VML (UM) served as the negative control and healthy muscle as the normal control (Ctrl). The overall workflow and defect-matching fabrication/implantation of VBP-printed constructs are illustrated in Fig. 6a, with representative intraoperative images confirming defect creation and stable scaffold placement (Fig. 6b).At 4 weeks, histological sections revealed clear group-dependent differences in tissue remodeling (Fig. 6c). H&E staining showed that the UM group exhibited a largely disorganized defect region with minimal muscle-like architecture, whereas scaffold-treated defects contained more cellular, tissue-like structures filling the defect space. Correspondingly, Masson's trichrome staining revealed extensive collagen deposition in the UM group, while collagen accumulation was noticeably reduced in scaffold-implanted groups, particularly in the porous scaffold conditions (P-G and P-G-MSCs) (Fig. 6c).

These observations suggest that a defect-filling matrix stabilizes the regenerative niche, and an interconnected porous architecture further facilitates host tissue infiltration, thereby reducing scar-dominated remodeling relative to untreated defects. By 8 weeks, the divergence between treatment groups became even more evident (Fig. 6d). UM defects remained dominated by collagen-rich fibrotic tissue, whereas porous scaffold implantation was associated with more organized muscle-like morphology within the defect region. Notably, the P-G-MSCs group displayed the most continuous muscle-like appearance and the least extensive collagen-rich areas among all treated groups (Fig. 6d), implying a synergistic benefit of the porous microstructure (supporting cell infiltration and integration) and MSC delivery (providing pro-regenerative paracrine cues). We further quantified the cross-sectional area (CSA) distribution of regenerating myofibers. The UM group was dominated by very small fibers, indicative of severe atrophy and impaired regeneration (Fig. 6e–h). Treatment with MSCs only or non-porous gel only slightly shifted the CSA distribution toward larger fibers, reflecting limited functional recovery. The P-G group induced a more pronounced rightward shift, consistent with improved maturation of regenerated fibers, likely because infiltrating cells experience a more physiological mechanical and nutritional environment within the pores. The P-G-MSCs group exhibited a CSA distribution profile that most closely resembled normal muscle, with a higher proportion of medium-to-large fibers and fewer atrophic fibers, indicating that the combination of porous architecture and MSCs most effectively restores muscle fiber size and maturation.

2.7 Porous MSC-laden hydrogel promoted vascularization and myogenic remodeling of regenerated muscle

To further elucidate the biological mechanisms underlying the improved structural regeneration observed in vivo, we performed immunofluorescence staining on TA defect sections(Fig. 7). To characterize immune cell modulation, we stained for M1-like pro-inflammatory macrophages ($CD86^+$) and M2-like pro-regenerative macrophages ($CD206^+$) at 4 and 8 weeks post-surgery. At 4 weeks, the UM group exhibited strong $CD86^+$ signals distributed throughout the defect region, indicating a pronounced pro-inflammatory microenvironment (Fig. 7a). In contrast, all treatment groups showed reduced $CD86^+$ staining, with the P-G and P-G-MSCs groups displaying the weakest signals. Quantification confirmed a significant reduction in CD86 intensity in P-G-MSCs compared to UM, with no significant difference between P-G and P-G-MSCs (Fig. 7e). By 8 weeks, this attenuation of pro-inflammatory signaling persisted (**Figure S11**): $CD86^+$ intensity in P-G-MSCs remained significantly lower than in UM, MSCs, and NP-G groups, and comparable to P-G, supporting sustained suppression of pro-inflammatory activity in porous scaffold conditions. In contrast to CD86, CD206 staining showed the opposite trend. At 4 weeks, $CD206^+$ signals were minimal in UM but became increasingly prominent in scaffold-treated defects, with the strongest signals observed in the P-G-MSCs group (Fig. 7b). Quantitative analysis confirmed significantly elevated $CD206^+$ intensity in P-G-MSCs relative to other groups (Fig. 7f). Importantly, this pro-regenerative marker remained highly expressed at 8 weeks, with P-G-MSCs continuing to show the strongest $CD206^+$ staining and intensity (**Figure S12**), suggesting that porous MSC-laden constructs promote M2 macrophage polarization and attenuate local inflammatory responses in vivo.

Additionally, platelet endothelial cell adhesion molecule-1 (CD31) immunofluorescence staining was conducted to assess the formation of newborn blood vessels. At 4 weeks, CD31-positive vascular structures were relatively sparse in the UM group, whereas scaffold-treated defects exhibited enhanced CD31 signals (Fig. 7c). In particular, the porous scaffold groups showed more apparent CD31-positive features, and P-G-MSCs displayed the most prominent CD31 staining among all groups. Consistently, quantitative analysis of fluorescence intensity confirmed that CD31 intensity in the P-G-MSCs group was markedly higher than in all other groups (Fig. 7g), suggesting that the porous MSC-laden constructs facilitate early neovascularization within the defect region. By 8 weeks, CD31 staining became more pronounced and organized in scaffold-treated groups, with P-G-MSCs still exhibiting the strongest CD31-positive signals (**Figure S13**), indicating a sustained pro-angiogenic effect of porous MSC-laden constructs during later-stage remodeling. To further assess vascular maturation within the defect region, we performed immunofluorescence staining for (α-SMA) to identify α-SMA$^+$ arterioles (mature vessels) (**Figure S14**). At 4 weeks, α-SMA$^+$ arteriole-like structures were relatively scarce in the UM group but became more evident in scaffold-treated defects, with the P-G-MSCs group showing the most prominent α-SMA staining. Quantification demonstrated a significantly increased number of α-SMA$^+$ arterioles in P-G-MSCs compared with UM and P-G. By 8 weeks, α-SMA$^+$ arterioles were detectable across all groups, and no significant differences were observed among treatments, suggesting that porous MSC-laden constructs primarily accelerate early-stage vascular maturation during VML repair.

To evaluate myogenic remodeling within the defect region, we performed myosin heavy chain (MHC) staining. At 4 weeks, the UM group showed weak and discontinuous MHC-positive signals, whereas scaffold implantation promoted broader and more continuous MHC-positive regions (Fig. 7d). Among all groups, P-G-MSCs displayed the most abundant and continuous MHC-positive areas, and quantification confirmed significantly higher MHC fluorescence intensity in P-G-MSCs (Fig. 7h), indicating enhanced formation of nascent skeletal muscle. By 8 weeks, MHC expression was further enhanced in all groups. Among them, the P-G-MSCs group exhibited the strongest MHC fluorescence intensity, confirming the positive regulatory effect of P-G-MSCs on VML repair (**Figure S15**).

2.8 MRI and ultrasound evaluation of defect restoration after VML

To non-invasively monitor longitudinal tissue remodeling following VML surgery, MRI and ultrasound imaging were performed at 4 and 8 weeks post-operation in all groups. Representative MRI images in coronal and sagittal planes, with enlarged defect region views, are presented in Fig. 8a-i (week 4) and Fig. 8b-i (week 8). At 4 weeks, the UM group showed a clearly identifiable defect characterized by disrupted tissue continuity and heterogeneous signal intensity relative to adjacent native muscle, consistent with incomplete bridging. In contrast, treatment groups exhibited varying degrees of defect filling, with a more compact tissue appearance and a less sharply demarcated boundary compared to UM. Among scaffold-based treatments, P-G and especially P-G-MSCs promoted more continuous, muscle-like morphology in both imaging planes, suggesting more advanced remodeling at this early

stage.By 8 weeks, MRI revealed progressive restoration of tissue integrity in treated defects (Fig. 8b-i). While UM defects remained readily identifiable with persistent structural discontinuity, scaffold-treated groups displayed further improvement in defect bridging and a trend toward more uniform muscle-like tissue. Notably, the P-G and P-G-MSCs groups exhibited the most substantial recovery of tissue continuity and morphology, approaching the structural characteristics of the Ctrl group more closely than UM and NP-G. Collectively, these longitudinal MRI observations indicate that defect-matching constructs support constructive remodeling over time, and a porous architecture—especially when combined with MSC delivery—further facilitates effective tissue regeneration.

Moreover, ultrasound imaging provided complementary, real-time assessment of tissue architecture and echotexture changes within the VML region (Fig. 8a**-ii and 8b-ii**). At week 4, the UM group displayed an obvious abnormal region with disorganized echogenic patterns compared with native muscle, whereas treated groups showed partial recovery of tissue continuity and a more integrated appearance across the defect site. Quantitative analysis of ultrasound images at week 4 (Fig. 8b-c) indicated that P-G-MSCs exhibited the highest mean grayscale values, showing better tissue continuity and less disrupted echogenicity compared to the UM and NP-G groups. At week 8, ultrasound images in scaffold-treated groups generally exhibited a more homogeneous echotexture and improved continuity of muscle-like structure, consistent with the remodeling trend observed by MRI. Quantitative ultrasound analysis at week 8 (Fig. 8e-f) showed that P-G-MSCs exhibited the highest mean grayscale values, reflecting superior tissue recovery, followed by P-G, MSCs, and NP-G, while UM showed the lowest values. These results suggest that P-G-MSCs facilitate the most advanced tissue restoration, as supported by both MRI and ultrasound.

2.9 Gait analysis of functional recovery in the operated hind limb

To evaluate functional recovery after VML repair, gait analysis was conducted at 8 weeks post-operation using an automated footprint-based gait recording system (workflow shown in Fig. 9a-b). All gait parameters were extracted from the operated hind paw. Representative footprint traces and corresponding contact-area curves demonstrated clear treatment-dependent differences in paw placement and stance dynamics (Fig. 9c). In the untreated VML group (UM), the operated hind paw showed reduced footprint contact and a smaller contact-area profile, consistent with compromised limb use. In contrast, scaffold-treated animals, particularly those receiving porous scaffolds (P-G and P-G-MSCs), showed a more apparent paw-print contact in the operated hind limb, as evidenced by a larger footprint contact area and higher contact-area curves (Fig. 9c). This increase in contact area suggests improved paw placement and more effective ground contact of the operated hind paw during gait, consistent with enhanced limb utilization after treatment.

Quantitative analyses further supported functional recovery (Fig. 9d–h). Compared with UM, stride length of the operated hind limb increased in scaffold-treated groups, with the porous scaffold + MSCs group (P-G-MSCs) showing the most pronounced improvement and approaching the Ctrl level (Fig. 9d).

Footprint (contact) area also increased after treatment (Fig. 9e), indicating enhanced contact formation of the operated hind paw during stance. Because reduced stride length and diminished contact area are commonly associated with protective gait and impaired limb function, the restoration of these metrics suggests improved locomotor performance and implies that structural repair of the defect site may contribute to more confident limb utilization during locomotion.

Temporal and phase-related parameters were also improved. UM animals showed shorter stance duration compared with Ctrl, indicating reduced time spent in ground contact by the operated hind paw (Fig. 9f). Treatment increased stance duration, and porous scaffold–based therapies produced the strongest recovery trend. Moreover, the propulsion index, which reflects the contribution of the operated hind limb during the push-off phase, was markedly elevated in porous scaffold groups, with P-G-MSCs showing the highest improvement among the treatments (Fig. 9g). The braking index, representing the deceleration/control phase during stance, also increased in scaffold-treated animals, with porous scaffold implantation yielding substantial restoration (Fig. 9h). Notably, the difference between P-G and P-G-MSCs appeared less prominent for braking than for propulsion, suggesting that scaffold architecture may be a major determinant for restoring stance control, while MSCs may provide additional benefit more strongly linked to overall stride performance and push-off capability. Collectively, gait analysis demonstrates persistent functional deficits in untreated VML animals at week 8, whereas porous gel scaffold implantation, especially when combined with MSCs, promotes measurable recovery of operated hind-limb gait dynamics.

3. Conclusion

In summary, this study demonstrates a robust VBP strategy for the reliable processing of ATPE bioinks into defect-matching, macroporous hydrogel constructs. By virtue of VBP's ultra-rapid, contactless, and perturbation-free volumetric photopolymerization, the internal emulsion microstructure can be effectively "locked in" before phase segregation, thereby extending the practical processing window of ATPE bioinks and maintaining uniform pore structures. Compared with conventional extrusion- and DLP-based bioprinting, VBP enables superior shape fidelity and spatially homogeneous microporosity throughout the entire construct. Importantly, pore size and porosity can be readily tailored by adjusting ATPE formulations and phase ratios, while diverse material combinations further broaden the achievable range of microstructures, mechanical properties, and degradation behaviors. Biologically, the VBP-printed porous hydrogels serve as a cytocompatible 3D microenvironment that supports high viability and proliferation of multiple cell types, while allowing pore-size-dependent cell organization, spreading, migration, and multicellular assembly. These beneficial effects are closely associated with enhanced mass transport and favorable contact guidance within the interconnected porous scaffold. When applied in a rat tibialis anterior VML model, implantation of the porous hydrogel constructs—especially when combined with MSCs—effectively promotes constructive tissue remodeling, reduces fibrotic scarring, and facilitates the formation of more mature muscle-like tissues, accompanied by improved imaging characteristics and functional gait recovery. Overall, the VBP-based processing of ATPE bioinks represents a versatile, scalable, and highly promising platform for fabricating high-fidelity macroporous

hydrogel scaffolds with broad applicability in tissue engineering and regenerative medicine. Future work will focus on optimizing the matching between scaffold degradation and tissue remodeling, promoting vascular and neural integration, and validating long-term functional outcomes in clinically relevant defect models, thereby further advancing the translational potential of this strategy.

4. Experimental Section

Material

Gelatin (V900863, Sigma-Aldrich), Polyvinyl Alcohol (563900, Sigma-Aldrich), Poly (ethylene glycol) (182001, Sigma-Aldrich), Dextran (D872024, Macklin), Poly (ethylene glycol) diacrylate (PEGDA) (EFL-PEGDA-1k, Engineering for Life), Pluronic F-127 (P822479, Macklin), Methacrylic anhydride (276685, Sigma-Aldrich), RU/SPS (5248-1KIT, Advanced BioMatrix), NHS-Fluorescein (46410, Thermo Scientific), Dimethyl sulfoxide (BS087, Biosharp), DMEM (Gibco), Serum-free medium for mesenchymal stem cells (CTCC-S019-HUM-M, Meisen CTCC), PBS (Gibco), Calcein/PI staining kit (C2015M, Beyotime), Cell Counting Kit-8 (C6005, New Cell & Molecular Biotech), PrestoBlue™ HS Cell Viability Reagent (P50200, Thermo Fisher), TRITC Phalloidin (40734ES75, Yeasen), DAPI (ES-8245, ECOTOP), Human umbilical vein endothelial cells (HUVEC-SV40) (SNL-503, SUNNCELL), NIH/3T3 (SNL-025, SUNNCELL), H9C2(SNL-029, SUNNCELL), Rat adipose derived mesenchymal stromal cell (ADSC), Print glass bottles (5-096-01, Maruemu, Japan), Confocal dishes (15mm, glass bottom, NEST).

Silk fibroin preparation

The Silk fibroin solutions were prepared according to the procedure reported by Kaplan et al [33]. Cocoons were cut into pieces and boiled in 0.02 M aqueous Na_2CO_3 solution for 30 min to remove SS from SF. Dissolve 40.35 g of LiBr in 500 mL of ultrapure water, then add 12.5 g of dried silk and react at 60°C for 4 hours until all the silk is completely dissolved. After the process, the solution is aliquot into dialysis bags (8–12 kDa), and the SF solution is collected after 3 days of dialysis.

Volumetric printing procedure: An ATPE bioink was prepared by mixing 10% (w/v) gelatin and 3% (w/v) PVA at a 3:1 (v/v) ratio and adding the photoinitiator system (0.5 mM Ru and 1 mM SPS). The ink was printed using volumetric bioprinter (VBP-T200, Grenn Key Biotech, China): the target geometry (STL file) was processed with the integrated slicing software and loaded into the printer, after which the bioink was transferred into a 1.2-cm-diameter transparent glass vial that was rotated about its longitudinal axis at 6.3° s^{-1} during exposure. For cell-laden printing, 3T3, H9c2, HUVECs, or MSCs were encapsulated in the gelatin/PVA ATPS bioink (1×10^6 cells mL^{-1}) and printed under the same initiator formulation (0.5 mM Ru/1 mM SPS) at a light intensity of 3 mW cm^{-2}.

Extrusion Printing and Digital Light Processing

For comparison with VBP, the same ATPE bioink formulation described above was used for both extrusion printing and digital light processing (DLP). For extrusion printing, the bioink was loaded into a 5

mL syringe barrel and pre-conditioned at 4°C for 10 min before being extruded and printed according to a pre-set program; the printed constructs were then UV-cured to complete crosslinking. For DLP printing, the prepared bioink was loaded into the resin vat and printed at a constant temperature of 37°C.

Structure similarity index measure

Structure similarity index measure (SSIM) is a measure of similarity for two samples, with arrange from 0 to 100%. The higher percentage means better similarity. The SSIM between the CADs and the resulting prints were calculated by a customized Matlab (R2020b, USA) program.

Morphology and Porosity Characterization

The cross-sectional morphology of volumetrically printed porous hydrogel constructs was examined by SEM (TM4000Plus II, Hitachi, Japan), with at least three images acquired from different fields of view for each sample. In parallel, porous microstructures were visualized by confocal fluorescence imaging, and the resulting 2D fluorescence images were quantified for pore size and porosity using ImageJ.

In Vitro Degradation Analysis

The initial dry weight of each hydrogel sample (W_0) was recorded, after which the samples were fully immersed in 1 mL PBS and incubated at 37°C under shaking (100 rpm). At predetermined time points (days 1–8), samples were collected, lyophilized, and weighed to obtain the remaining dry weight (W□). The percentage of remaining mass (degradation rate) was calculated using

$$Degradation\ rate\ (\%) = \frac{Wt}{W0} \times\ 100\%$$

Mechanical property measurement

The compressive properties of the porous hydrogels were measured using a mechanical testing system (TA.XT Plus C, Stable Micro Systems, UK). Each sample was tested in triplicate (three independent parallel measurements).

Biocompatibility and Cell Proliferation Assays: The biocompatibility of the porous hydrogels was assessed using Live/Dead staining with H9c2, 3T3, and MSCs. Briefly, cells (1 × 10^6 cells mL^{-1}) were mixed with the hydrogel precursor solution and crosslinked by VBP. After printing, constructs were washed with sterile PBS to remove unincorporated components and then cultured in complete DMEM. Live/Dead staining was performed on days 1, 4, and 7 using a Calcein/PI kit (30 min incubation), and fluorescence images were acquired using a fluorescence microscope (MF53-N, MSHOT, China), where live and dead cells were identified by green and red fluorescence, respectively. Cell proliferation within the porous hydrogels was evaluated using a CCK-8 assay. Cell-laden constructs were incubated with 10% (v/v) CCK-8 solution for 1 h at 37°C on days 1, 4, and 7, and absorbance at 450 nm (OD_{450}) was measured using a microplate reader (BioTek Synergy LX, Agilent, USA). In addition, metabolic activity was quantified using the PrestoBlue reagent following the manufacturer's instructions. After three PBS washes, constructs

were transferred to 24-well plates and incubated with a medium/working solution mixture (9:1, v/v) for 3 h at 37°C; the supernatants were then read on a spectrophotometer (BioTek Synergy LX, Agilent, USA) at 570 nm excitation and 600 nm emission.

Immunofluorescence Staining

HUVECs and MSCs (each at 1 × 10^6 cells mL^{-1}) were encapsulated in porous hydrogels by volumetric bioprinting and cultured for 1, 4, and 7 days. At each time point, samples were washed with PBS, fixed in 4% paraformaldehyde for 15 min, and permeabilized with 0.5% Triton X-100 for 10 min. F-actin was stained by incubating the constructs with rhodamine–phalloidin (100 nM) for 30 min at room temperature, followed by nuclear counterstaining with DAPI (100 nM) for 5 min. Fluorescence images were acquired using a confocal microscope (LSM900, ZEISS, Germany).

Experimental Animals and Ethical Statement: All animal experiments were approved by the Animal Ethics Committee of West China Hospital, Sichuan University (Approval No: 20260210001). and conducted in strict accordance with the institutional guidelines for the care and use of laboratory animals. Sixty healthy adult female Sprague-Dawley (SD) rats (8 weeks old, weighing approximately 250 g) were obtained from Byrness Weil biotech Ltd. All rats were housed in a Specific-Pathogen-Free (SPF) facility under controlled conditions (23 ± 2°C, 50 ± 10% humidity) with a 12-hour light/dark cycle. Standard pellet chow and water were available ad libitum. The animals were allowed to acclimatize for one week prior to any procedures.

Construction of the rat Volumetric Muscle Loss (VML) model: All surgical procedures were performed under aseptic conditions. Anesthesia was induced and maintained using isoflurane inhalation. Once deeply anesthetized, the hair on the right hindlimb was shaved, and the surgical site was disinfected with povidone-iodine solution. A longitudinal skin incision was made parallel to the femur, followed by blunt dissection of the fascia to fully expose the underlying vastus lateralis muscle. A full-thickness, cylindrical defect (5 mm in diameter and 5 mm in depth) was created in the mid-belly of the vastus lateralis muscle using a 5 mm sterile biopsy punch. Rats were randomly allocated into six groups (n = 10/group): (1) Normal: no VML defect; (2) Control: Only VML defect; (3) Cell therapy: A suspension of 2×10^6 ADSCs in 80 μL of vehicle was injected directly into the VML defect; (4) Non-porous hydrogel: A sterile, cylindrical non-porous hydrogel scaffold (Φ5 mm × 5 mm) was implanted into the VML defect; (5) 120 μm porous hydrogel: A sterile, cylindrical 120 μm porous hydrogel scaffold (Φ5 mm × 5 mm) was implanted into the VML defect; (6) 120 μm porous hydrogel + ADSCs: A 120 μm porous hydrogel scaffold (Φ5 mm × 5 mm) pre-seeded with 2×10^6 ADSCs was implanted into the VML defect. All implants were carefully positioned to completely fill the defect. Subsequently, the overlying muscle fascia was closed with 5 − 0 absorbable sutures using an interrupted pattern to secure the implant. Finally, the skin incision was closed with 3 − 0 non-absorbable interrupted sutures.

Post-operative Care

Immediately after surgery, rats were placed on a heating pad to maintain body temperature until they fully recovered from anesthesia. To provide post-operative analgesia and for infection prophylaxis, meloxicam and penicillin potassium injection were administered subcutaneously for three consecutive days. Animals were monitored daily for general health, food and water intake, mobility, and for any signs of surgical site complications, such as inflammation, exudation, or infection.

Histological and Immunofluorescence Analysis

At 4 and 8 weeks post-surgery, the targeted vastus lateralis muscles encompassing the defect regions were meticulously excised following euthanasia. The harvested specimens were fixed in 4% paraformaldehyde at 4°C for 24 hours, dehydrated through a graded ethanol series, embedded in paraffin, cut into 5 μm sections with a microtome, and placed in a 65°C oven for 6 h. Before histological staining, the muscle tissue sections were placed in xylene for 40 min to remove paraffin, and subsequently rehydrated through a graded ethanol series to distilled water. H&E and Masson's trichrome staining were performed according to the manufacturer’s instructions to evaluate general morphological regeneration and the extent of fibrosis (collagen deposition), respectively. To assess muscle fiber maturation quantitatively, the cross-sectional area (CSA) of regenerating neonatal myofibers was calculated from the H&E images using ImageJ software. All histochemically stained slides were digitized utilizing a whole-slide imaging system (VS200, Olympus, Japan). For immunofluorescence profiling, the paraffin sections underwent deparaffinization and rehydration. Antigen retrieval was then performed using a pH 8.0 retrieval solution via microwave heating on high power for 8 min, which was repeated twice. After blocking non-specific binding sites with 5% bovine serum albumin (BSA) for 1 hour at room temperature, the sections were incubated overnight at 4°C with specific primary antibodies, including CD86 (rabbit anti-CD86, HUABIO, ER1906-01), CD206 (mouse anti-CD206, HUABIO, HA601453), CD31 (rabbit anti-CD31, ABclonal, A19014), α-Smooth Muscle Actin (mouse anti-α-SMA, Proteintech, 67735-1-Ig) and myosin heavy chain (mouse anti-MHC, Abcam, ab37484). Following incubation with corresponding fluorophore-conjugated secondary antibodies and nuclear counterstaining with DAPI, high-resolution fluorescent images were captured using a whole-slide imaging system (VS200, Olympus, Japan). The quantitative analysis of the mean fluorescence intensities for the targeted markers was performed using ImageJ software.

Ultrasound and Magnetic Resonance Imaging (MRI)

Longitudinal tissue remodeling, defect bridging, and morphological integration within the quadriceps (vastus lateralis) muscle were monitored using ultrasound and MRI at 4 and 8 weeks post-operation. During all imaging procedures, rats were anesthetized with vaporized isoflurane. For ultrasound evaluation, the hindlimb was depilated using a hair removal cream, and ultrasonic gel was applied. High-resolution ultrasound imaging (Vevo 3100, FUJIFILM VisualSonics, Canada) was conducted in both the coronal and sagittal planes. The echotexture and structural continuity of the regenerating tissue were evaluated, and the mean grayscale values within the defect regions were quantified using ImageJ software (NIH, USA) to objectively assess tissue density recovery. Subsequently, MRI scans were

acquired using a 7.0 T small animal MRI scanner (BioSpec 70/30 USR, Bruker, Germany). Representative MRI images in the coronal and sagittal planes were captured to visualize morphological restoration, evaluate the attenuation of the defect boundary, and examine the structural continuity of the regenerating muscle in comparison to the adjacent native tissue.

Gait Analysis

To evaluate the functional recovery of the operated hind limbs after vastus lateralis VML injury and subsequent treatments, an automated footprint-based gait analysis system (GAT-100 Gait Analysis System, Chengdu Taimeng Software Co., Ltd.) was employed at 8 weeks post-surgery. Before the formal experiment, the rats were acclimated and trained for 3 days to ensure they could cross the defined transparent walkway without hesitation at a relatively constant speed. A high-speed camera positioned beneath the glass plate continuously recorded the walking videos of the rats in their natural state without interruption. The analysis process consisted of interactively categorizing the points of contact for each limb (right forepaw, left forepaw, right hindpaw, and left hindpaw). Based on the captured videos, the spatial and temporal gait parameters of the operated hind paws were extracted and calculated using the accompanying visual analysis system software. To quantitatively assess the restoration of locomotor performance and limb utilization, key metrics including stride length, footprint (contact) area, stance duration, propulsion index, and braking index were analyzed and compared across all groups.

Declarations

Conflict of Interest

The authors declare no conflict of interest.

Data Availability Statement

The data that support the findings of this study are available from the corresponding author upon reasonable request.

References

1. Daly A. C., Prendergast M. E., Hughes A. J., Burdick1 J. A. Bioprinting for the Biologist. *Cell* **184**, 18-32 (2021).
2. Tang G.*, et al.* Liquid-embedded (bio)printing of alginate-free, standalone, ultrafine, and ultrathin-walled cannular structures. *P. Natl. Acad. Sci. Usa* **120**, e2206762120 (2023).
3. Lee S. J., Jeong W., Atala A. 3D Bioprinting for Engineered Tissue Constructs and Patient-Specific Models: Current Progress and Prospects in Clinical Applications. *Adv. Mater.* **36**, 2408032 (2024).

4. Huang W.*, et al.* Nanoengineered extrusion-aligned tract bioprinting enables functional repair of spinal cord injuries. *Cell Stem Cell* **33**, 1-15 (2026).
5. Choi S.*, et al.* Fibre-infused gel scaffolds guide cardiomyocyte alignment in 3D-printed ventricles. *Nat. Mater.* **22**, 1039-1046 (2023).
6. Van Belleghem S.*, et al.* Hybrid 3D Printing of Synthetic and Cell-Laden Bioinks for Shape Retaining Soft Tissue Grafts. *Adv. Funct. Mater.* **30**, 1907145 (2019).
7. Wu H.*, et al.* Hydrogel-based 3D printing technology: From interfacial engineering to precision medicine. *Adv. Colloid Interface Sci.* **341**, 103481 (2025).
8. Lu P.*, et al.* Harnessing the potential of hydrogels for advanced therapeutic applications: current achievements and future directions. *Signal Transduction Targeted Ther.* **9**, 166 (2024).
9. Cao H., Duan L., Zhang Y., Cao J., Zhang K. Current hydrogel advances in physicochemical and biological response-driven biomedical application diversity. *Signal Transduction Targeted Ther.* **6**, 426 (2021).
10. Zauchner D.*, et al.* Synthetic biodegradable microporous hydrogels for in vitro 3D culture of functional human bone cell networks. *Nat. Commun.* **15**, 5027 (2024).
11. Wu H.*, et al.* Injectable micropore-forming microgel scaffold for neural progenitor cells transplantation and vascularization after stroke. *Nat. Commun.* **16**, 9285 (2025).
12. He S.*, et al.* Robust super-structured porous hydrogel enables bioadaptive repair of dynamic soft tissue. *Nat. Commun.* **16**, 3198 (2025).
13. Feng Y., Ringeisen N., Dufresne E. R., Isa L., Style R. W. Controlling Polymerization-Induced Phase Separation in the Synthesis of Porous Gels. *ACS Nano* **19**, 41718-41726 (2025).
14. Lloyd E. C.*, et al.* Porous hierarchically ordered hydrogels demonstrating structurally dependent mechanical properties. *Nat. Commun.* **16**, 3792 (2025).
15. Liu Y., Suarez-Arnedo A., Caston E. L. P., Riley L., Schneider M., Segura T. Exploring the Role of Spatial Confinement in Immune Cell Recruitment and Regeneration of Skin Wounds. *Adv. Mater.* **35**, 2304049 (2023).
16. Lowen J. M.*, et al.* Functionalized Annealed Microgels for Spatial Control of Osteogenic and Chondrogenic Differentiation. *Adv. Funct. Mater.* **34**, 2311017 (2024).
17. Wu J.*, et al.* Fishing out AIEC with FimH capturing microgels for inflammatory bowel disease treatment. *Nat. Commun.* **16**, 7924 (2025).
18. Liu Z.*, et al.* Microgel-Based Hierarchical Porous Hydrogel Patch with Adhesion and Resilience for Myocardial Infarction. *Adv. Sci.* **13**, e18646 (2026).
19. Ying G.-L.*, et al.* Aqueous Two-Phase Emulsion Bioink-Enabled 3D Bioprinting of Porous Hydrogels. *Adv. Mater.* **30**, e1805460 (2018).
20. Xue W.*, et al.* A Facile Strategy for the Fabrication of Cell-laden Porous Alginate Hydrogels Based on Two-phase Aqueous Emulsions. *Adv. Funct. Mater.* **33**, 2214129 (2023).

21. Messaoud G. B., Aveic S., Wachendoerfer M., Fischer H., Richtering W. 3D Printable Gelatin Methacryloyl (GelMA)-Dextran Aqueous Two-Phase System with Tunable Pores Structure and Size Enables Physiological Behavior of Embedded Cells In Vitro. *Small* **19**, e2208089 (2023).
22. Joseph T. Toombs M. L., Caitlyn C. Cook, Sophie Jenne, Chi Chung Li, Bastian E. Rapp, Frederik Kotz-Helmer, Hayden K. Taylor. Volumetric additive manufacturing of silica glass with microscale computed axial lithography. *Science* **376**, 308–312 (2022).
23. Xie M.*, et al.* Volumetric additive manufacturing of pristine silk-based (bio)inks. *Nat. Commun.* **14**, 210 (2023).
24. Florczak S.*, et al.* Adaptive and context-aware volumetric printing. *Nature* **645**, 108-114 (2025).
25. Bernal P. N.*, et al.* Volumetric Bioprinting of Complex Living-Tissue Constructs within Seconds. *Adv. Mater.* **31**, 1904209 (2019).
26. Lian L.*, et al.* Rapid Volumetric Bioprinting of Decellularized Extracellular Matrix Bioinks. *Adv. Mater.* **36**, 2304846 (2024).
27. Bernal P. N.*, et al.* The road ahead in materials and technologies for volumetric 3D printing. *Nat. Rev. Mater.* **10**, 826–841 (2025).
28. Brian M. Sicari J. P. R., Christopher L. Dearth, Matthew T. Wolf, Fabrisia Ambrosio, Michael Boninger, Neill J. Turner, Douglas J. Weber, Tyler W. Simpson, Aaron Wyse, Elke H. P. Brown, Jenna L. Dziki, Lee E. Fisher, Spencer Brown, Stephen F. Badylak. An Acellular Biologic Scaffold Promotes Skeletal Muscle Formation in Mice and Humans with Volumetric Muscle Loss. *Sci. Transl. Med.* **6**, 234 (2014).
29. Corona B. T., Rivera J. C., Owens J. G., Wenke J. C., Rathbone C. R. Volumetric muscle loss leads to permanent disability following extremity trauma. *J. Rehabil. Res. Dev.* **52**, 785-792 (2015).
30. Grogan B. F. H., Joseph R. Volumetric Muscle Loss. *J. Am. Acad. Orthop. Surg.* **19**, S35-S37 (2011).
31. Qazi T. H., Duda G. N., Ort M. J., Perka C., Geissler S., Winkler T. Cell therapy to improve regeneration of skeletal muscle injuries. *J. Cachexia. Sarcopeni.* **10**, 501-516 (2019).
32. Li H.*, et al.* Customized platelet-rich plasma with transforming growth factor β1 neutralization antibody to reduce fibrosis in skeletal muscle. *Biomaterials* **87**, 147-156 (2016).
33. Pritchard E. M., Hu X., Finley V., Kuo C. K., Kaplan D. L. Effect of Silk Protein Processing on Drug Delivery from Silk Films. *Macromol. Biosci.* **13**, 311-320 (2013).

Schemes

Scheme 1 is available in the Supplementary Files section

Figures

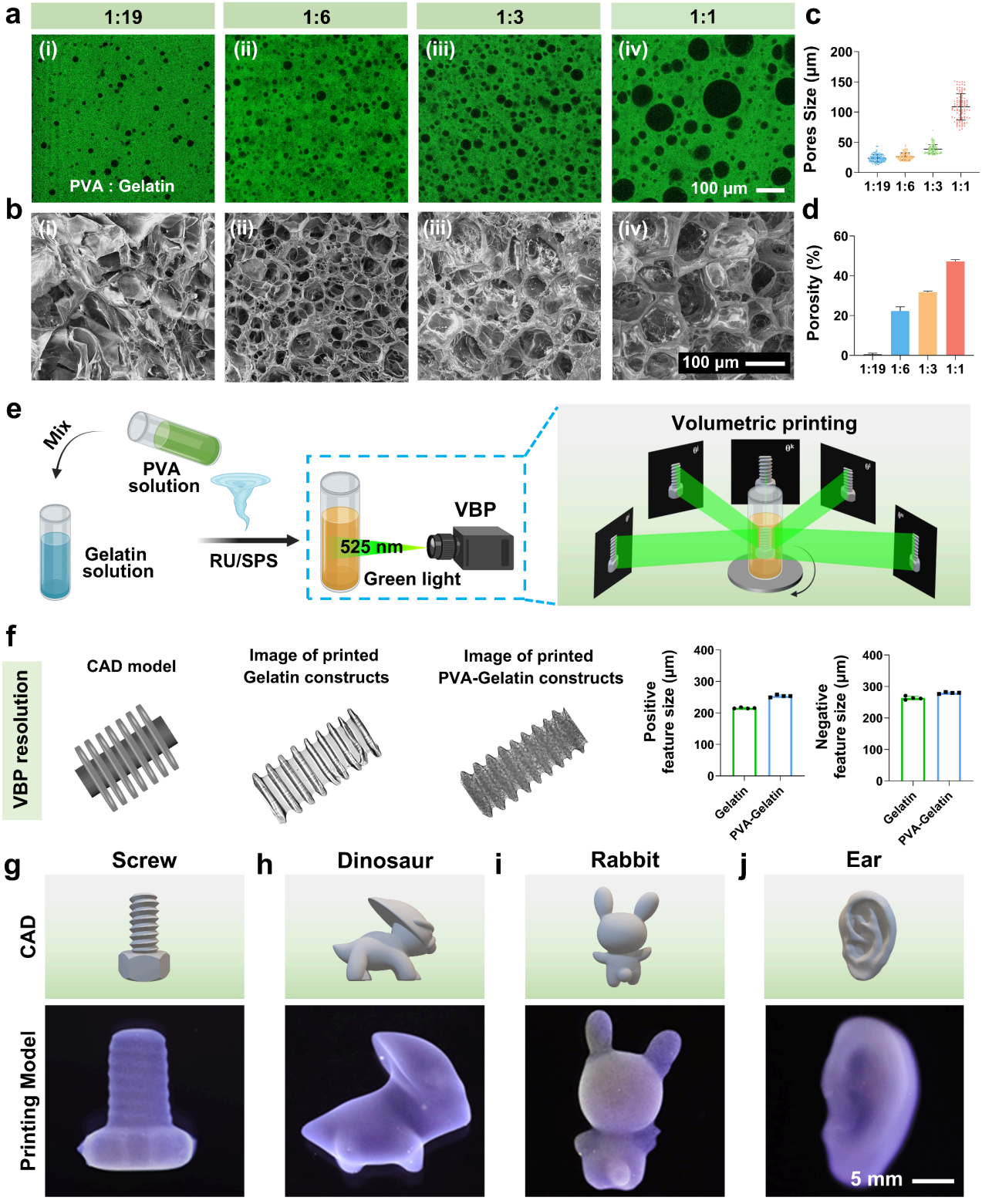


Figure 1

Fabrication and characterization of PVA–gelatin-based emulsion bioink and porous constructs printing. a-b) Fluorescence microscopy (a) and corresponding SEM images (b) of PVA–gelatin-based emulsion bioink with varying volumetric ratios (1:19, 1:6, 1:3, 1:1). The green channel represents the gelatin phase, and dark voids correspond to pores. Scale bar: 100 μm. c-d) Quantitative analysis of average pore size (c) and porosity (d) for each formulation. e) Schematic diagram of PVA-gelatin-based

emulsion bioink VBP process. f) VBP resolution analysis of gelatin-only and gelatin–PVA emulsion bioinks. g-j) Representative 3D constructs fabricated via VBP using PVA–gelatin emulsion bioinks, including a screw (g), dinosaur (h), rabbit (i), and ear (j). CAD models (top) and corresponding printed models (bottom) are shown.

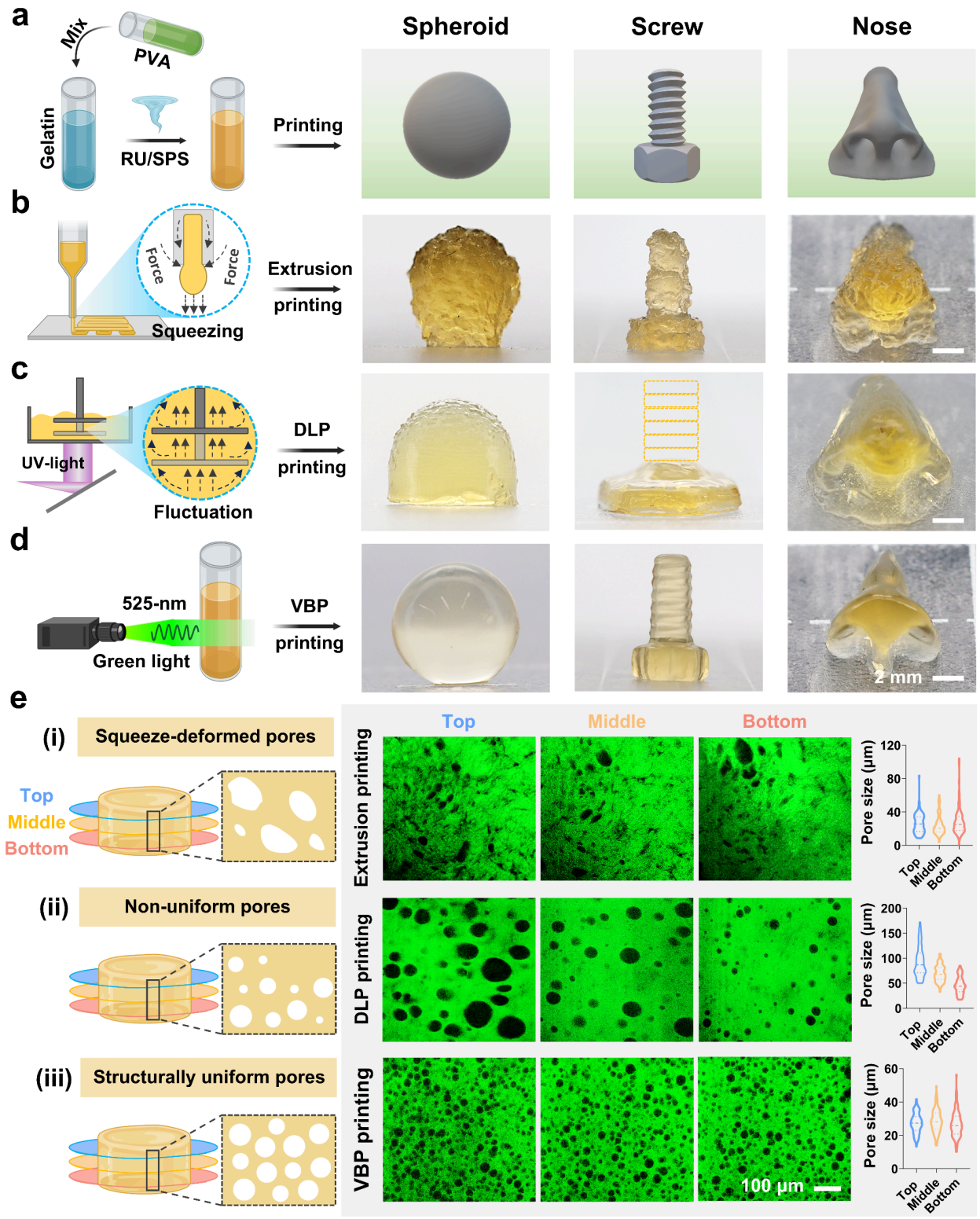


Figure 2

Fabrication and characterization of PVA–gelatin-based emulsion bioink and porous constructs printing. a) Preparation of PVA–gelatin ATPE bioink and schematic CAD models (spheroid, screw, and nose) used as standardized printing geometries. b-d) Schematic illustrations of extrusion (b), DLP (c), and VBP (d) printing of the ATPE bioink and corresponding photographs of the printed constructs. e) Comparison of internal microporous structures formed by different printing strategies. (i) Extrusion-printed constructs exhibit squeezed and deformed pores across the height. (ii) DLP-printed constructs show non-uniform pores with pronounced size gradients from top to bottom. (iii) VBP-printed constructs maintain structurally uniform, near-spherical pores throughout the entire construct. Confocal images are shown for top, middle, and bottom regions, with corresponding pore-size quantification on the right.

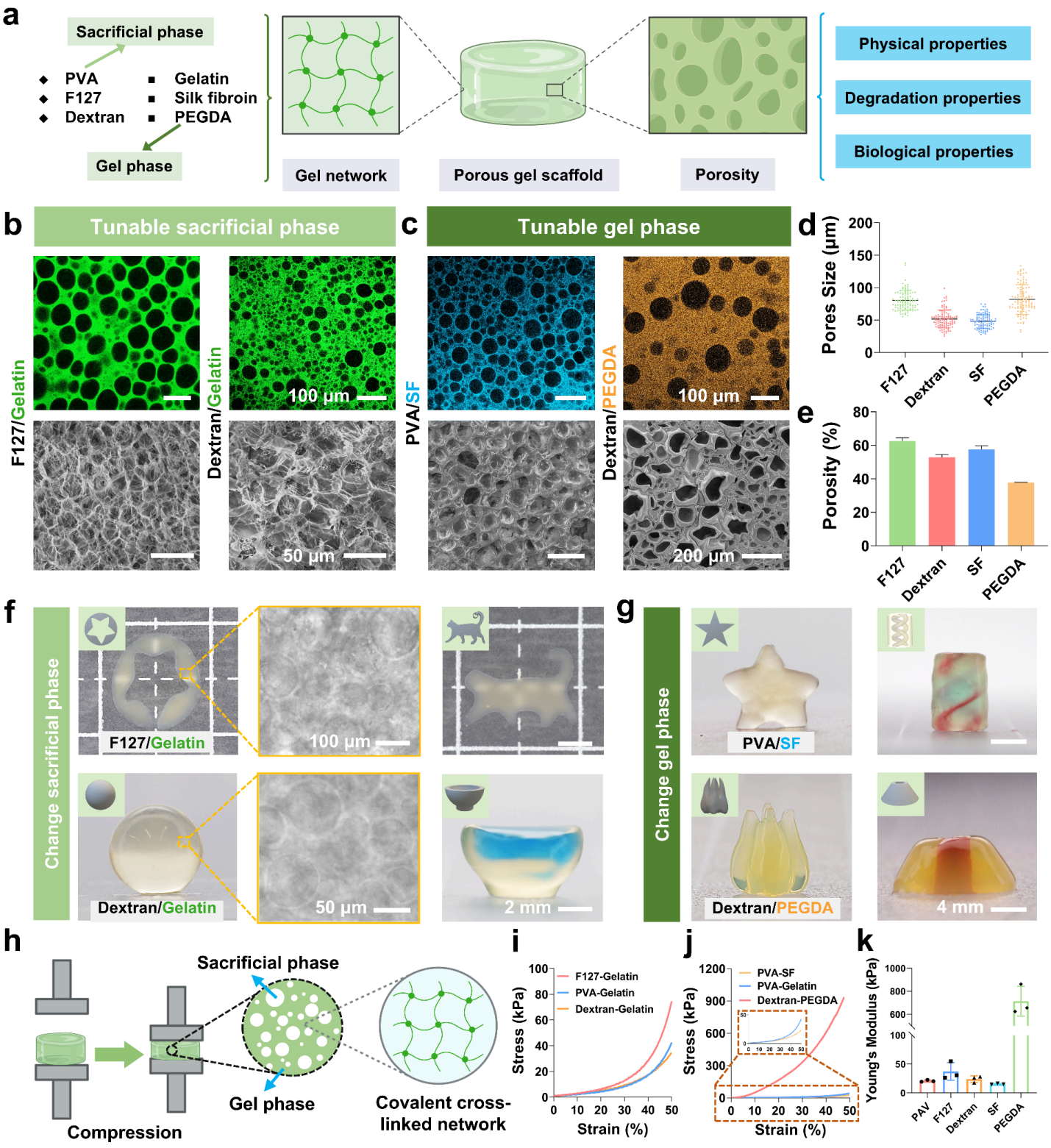


Figure 3

Effects of different ATPE bioink combinations on microstructure regulation, print fidelity, and mechanical properties of VBP-printed macroporous hydrogels. a) Schematic illustration of ATPE design, in which different sacrificial phases (PVA, F127, dextran) and gel-forming phases (gelatin, SF, PEGDA) are combined to generate porous gel scaffolds with tunable physical, degradation, and biological properties. b) Confocal fluorescence images and corresponding SEM micrographs of gelatin-

based scaffolds prepared with F127 or dextran as the sacrificial phase. c) Confocal fluorescence images and SEM micrographs of scaffolds prepared with alternative gel-forming phases (SF and PEGDA). d-e) Quantitative analysis of pore size (d) and porosity (e) for different ATPE bioink combinations. f) Representative VBP-printed constructs obtained from F127/gelatin and dextran/gelatin ATPE bioinks, with enlarged views of their internal microporous structures. g) Representative VBP-printed constructs obtained from PVA/SF and dextran/PEGDA ATPE bioinks. h) Schematic of uniaxial compression testing of the printed porous gel scaffolds. i-j) Stress–strain curves for scaffolds with different sacrificial (i) and gel (j) phases. k) Young‘s modulus of scaffolds derived from various ATPE compositions.

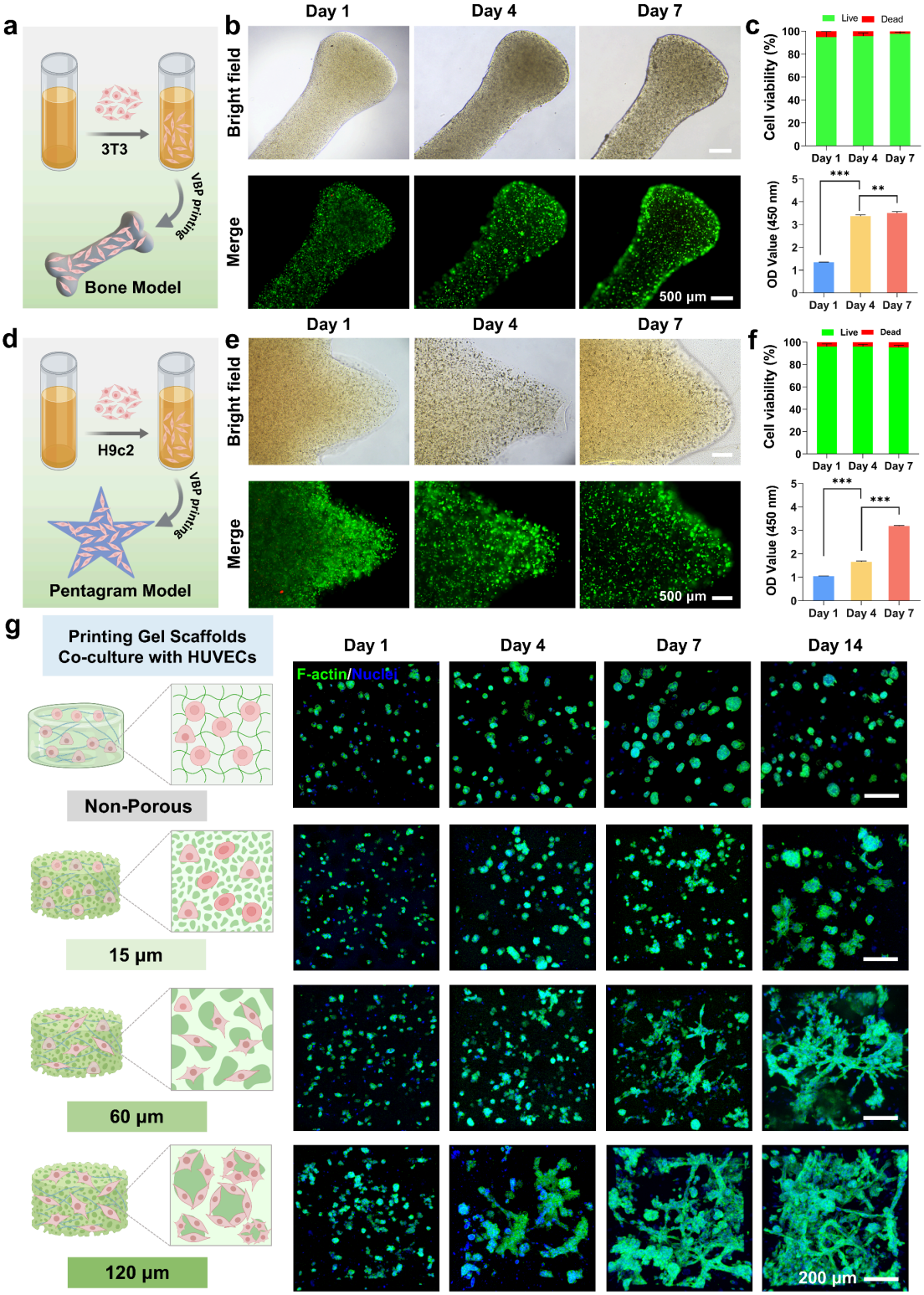


Figure 4

Evaluation of cell viability, proliferation, and endothelial organization in VBP-printed PVA/gelatin ATPE scaffolds. a, d) Schematic of printed constructs (bone-shaped for 3T3 cells; star-shaped for H9c2 cells). b, e) Live/Dead fluorescence images (green = live, red = dead) at days 1, 4, and 7 show nearly all cells remained alive (representative images for 3T3 in bone construct and H9c2 in star construct). c, f) Quantitative viability (~95–99% live cells) and metabolic activity (OD 450 nm) at days 1, 4, 7 for 3T3 and

H9c2, indicating high viability and significant cell proliferation over 7 days. g) Schematic of HUVEC co-culture on non-porous and porous PVA/gelatin scaffolds with different pore sizes (non-porous, ~15 μm, ~60 μm, ~120 μm), and representative F-actin (green)/nuclei (blue) fluorescence images on days 1, 4, 7, and 14. Data are presented as mean ± SD (n = 3 biologically independent samples). ***P < 0.001, **P < 0.002, *P < 0.033, ns: no significant difference, one-way ANOVA.

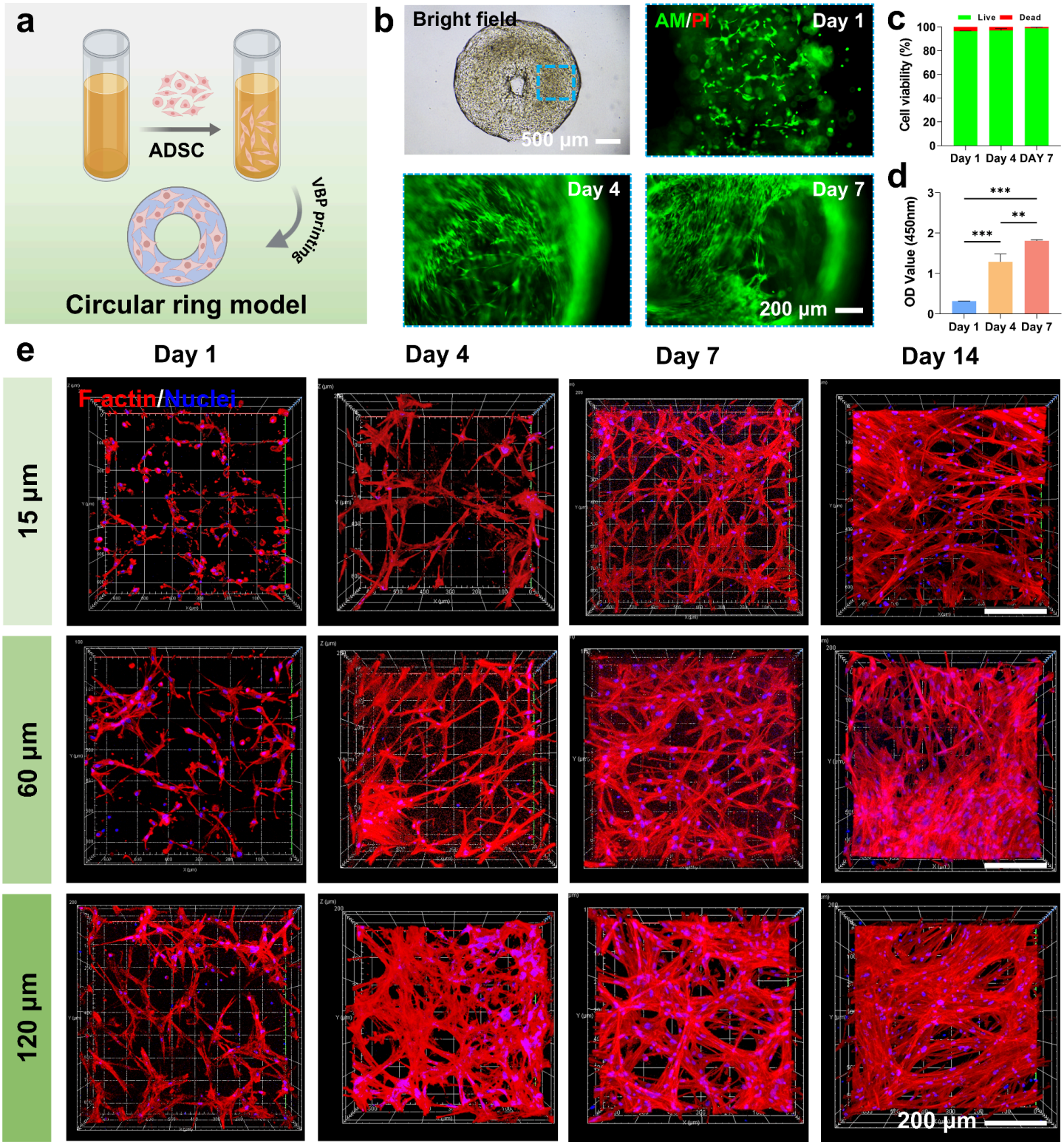


Figure 5

Evaluation of MSCs viability, proliferation, and cytoskeletal organization in VBP-printed PVA/gelatin scaffolds with different pore sizes. a) Schematic illustration of VBP printing of MSCs-laden PVA/gelatin ATPE bioink into a circular ring-shaped construct. b) Bright-field and Live/Dead fluorescence images of MSCs-laden ring constructs on days 1, 4, and 7. c-d) Quantification of MSCs viability (c) and metabolic activity (d) on days 1, 4, and 7. e) Confocal 3D reconstructions of MSCs cultured in scaffolds with different pore sizes (~15 μm, ~60 μm, ~120 μm) at days 1, 4, 7, and 14 (DAPI: blue; F-actin: Red). Data are presented as mean ± SD (n = 3 biologically independent samples). ***P < 0.001, **P < 0.002, *P < 0.033, ns: no significant difference, one-way ANOVA.

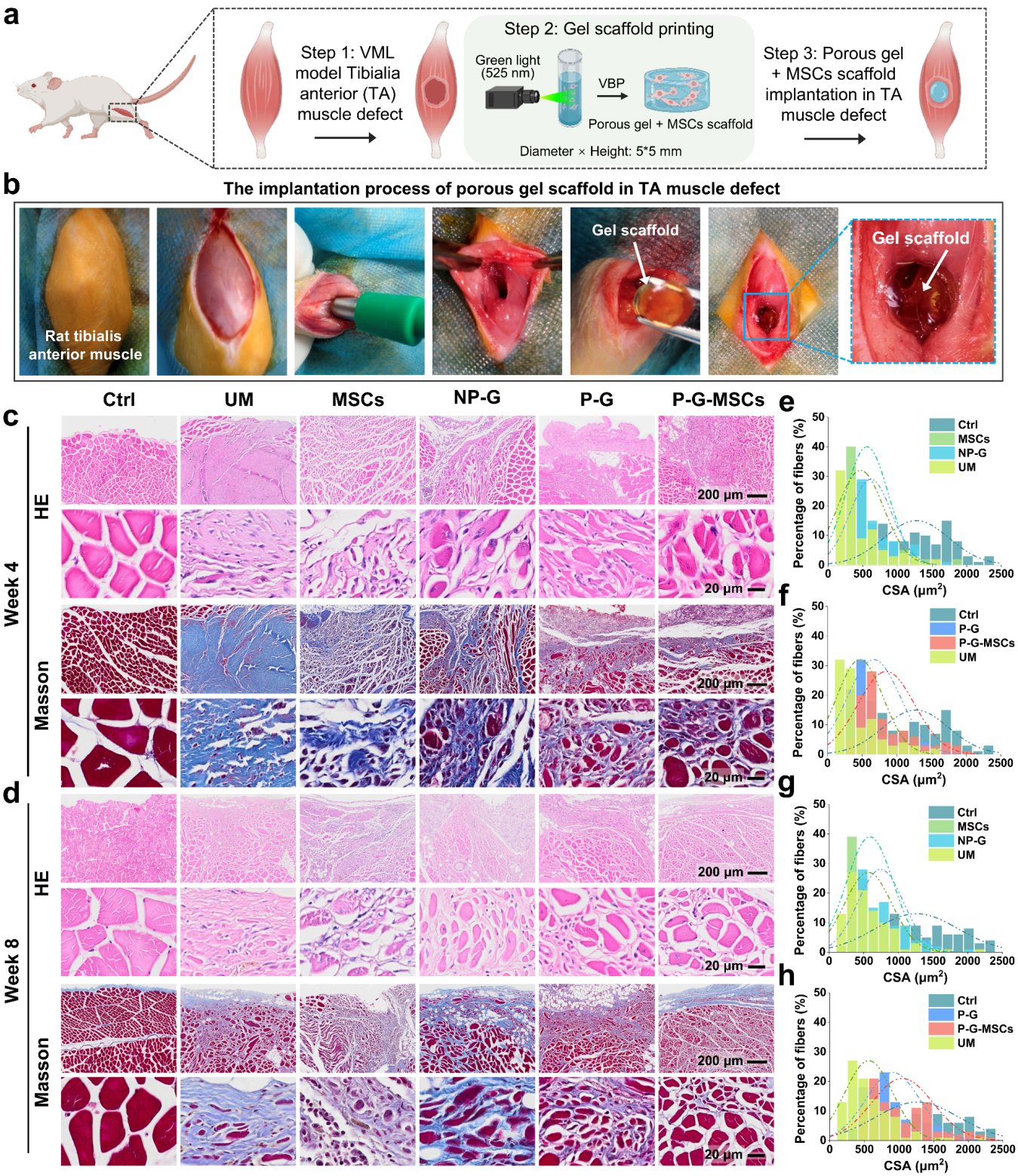


Figure 6

In vivo evaluation of VBP-printed porous MSCs-laden gel scaffolds in a rat TA VML model. a) Schematic of TA VML defect creation (5 mm diameter × 5 mm height) and porous MSCs-laden scaffold implantation. b) Representative photographs showing TA exposure, defect creation, and scaffold implantation in the defect site. c-d) H&E and Masson staining images of the defect region at 4 weeks (c) and 8 weeks (d) post-surgery for each group. Scale bars: 200 μm (low magnification) and 20 μm (high

magnification). e-h) Frequency distribution statistics of the cross-sectional area (CSA) of neonatal myofibers at 4 (e-f) and 8 (g-h) weeks, shown for the indicated group comparisons (n=3 biologically independent samples). Ctrl: Normal group, UM: untreated VML group, MSCs: MSCs only group, NP-G: non-porous gel group, P-G: porous gel group, P-G-MSCs: porous gel + MSCs group.

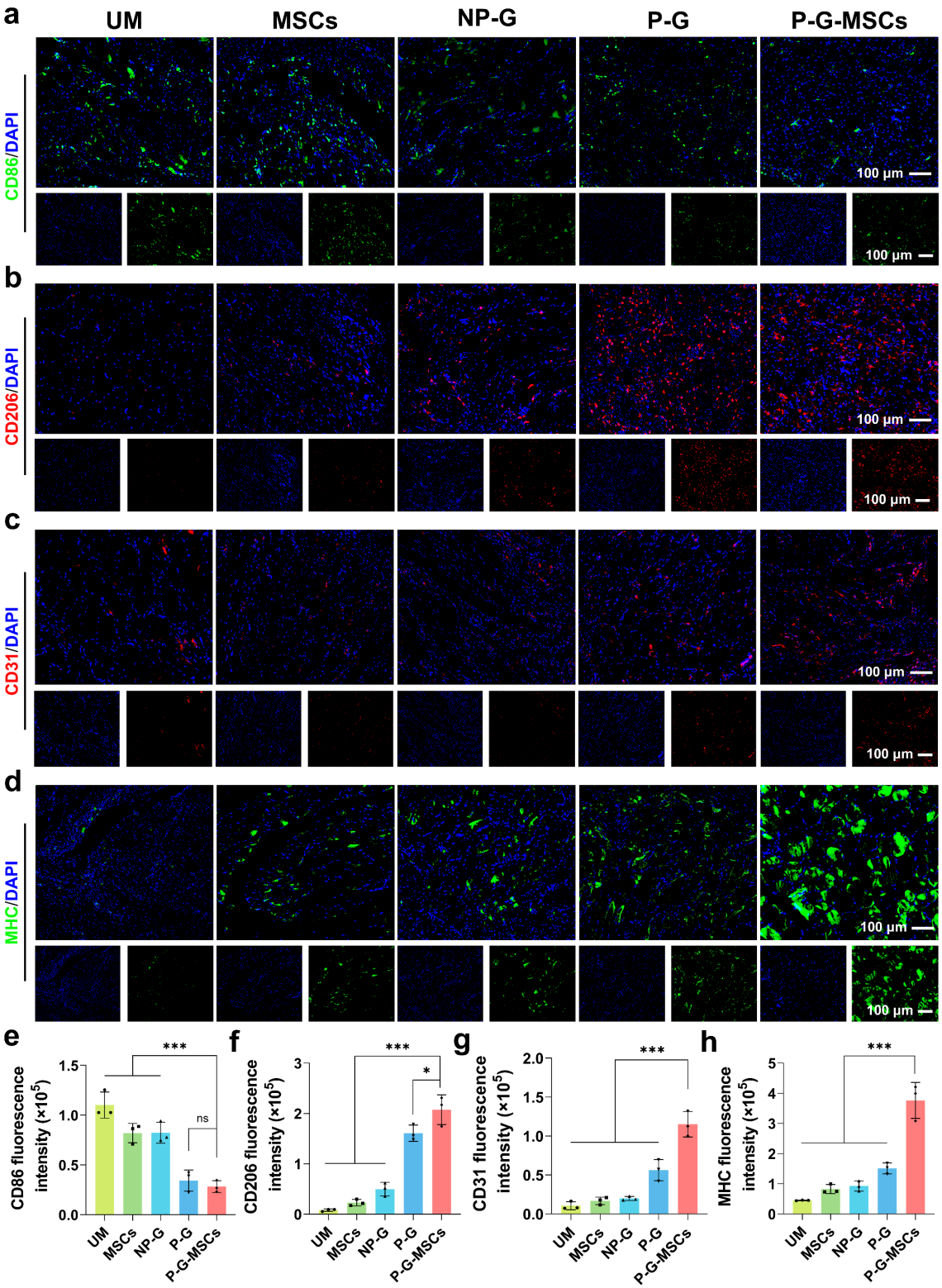


Figure 7

Immunofluorescence evaluation of macrophage phenotype–associated signals, neovascularization, and myogenic remodeling in the TA defect region at 4 weeks after VML treatment. a-d) Representative immunofluorescence images of CD86 (a), CD206 (b), CD31 (c) and MHC (d) for UM, MSCs, NP-G, P-G, and P-G-MSCs groups at 4 weeks (CD86: green; CD206: red; CD31: red; MHC: green; DAPI: blue; corresponding single channels are shown below). e-h) Quantitative analysis of the fluorescence intensity of CD86 (e), CD206 (f), CD31 (g) and MHC (h), respectively. Data are presented as mean ± SD (n = 3 biologically independent samples). ***P < 0.001, **P < 0.002, *P < 0.033, ns: no significant difference, one-way ANOVA.

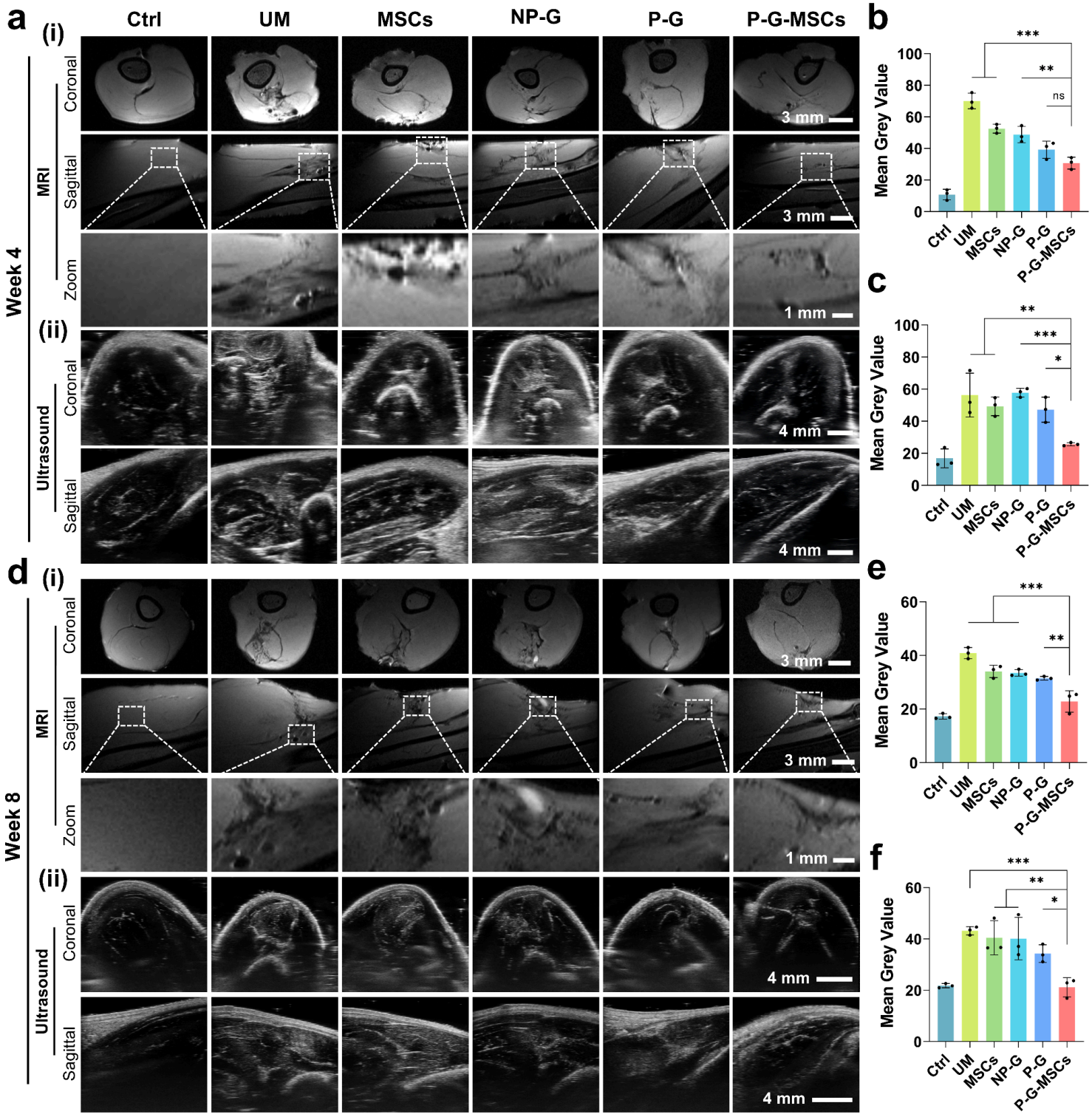


Figure 8

MRI and ultrasound evaluation of TA muscle remodeling after VML treatment. a) Representative MRI (i) images (coronal and sagittal, with enlarged views of the defect region) and ultrasound (ii) images (coronal and sagittal) at week 4 post-operation for Ctrl, UM, MSCs, NP-G, P-G, and P-G-MSCs groups. b-c) Quantitative analysis of mean grayscale values from ultrasound images at week 4 from coronal (c) and sagittal (d) images, respectively. d) Representative MRI (i) and ultrasound (ii) images at week 8 post-operation. e-f) Quantitative analysis of mean grayscale values from ultrasound images at week 8 from coronal (e) and sagittal (f) images, respectively. Data are presented as mean ± SD (n = 3 biologically independent samples). ***P < 0.001, **P < 0.002, *P < 0.033, ns: no significant difference, one-way ANOVA.

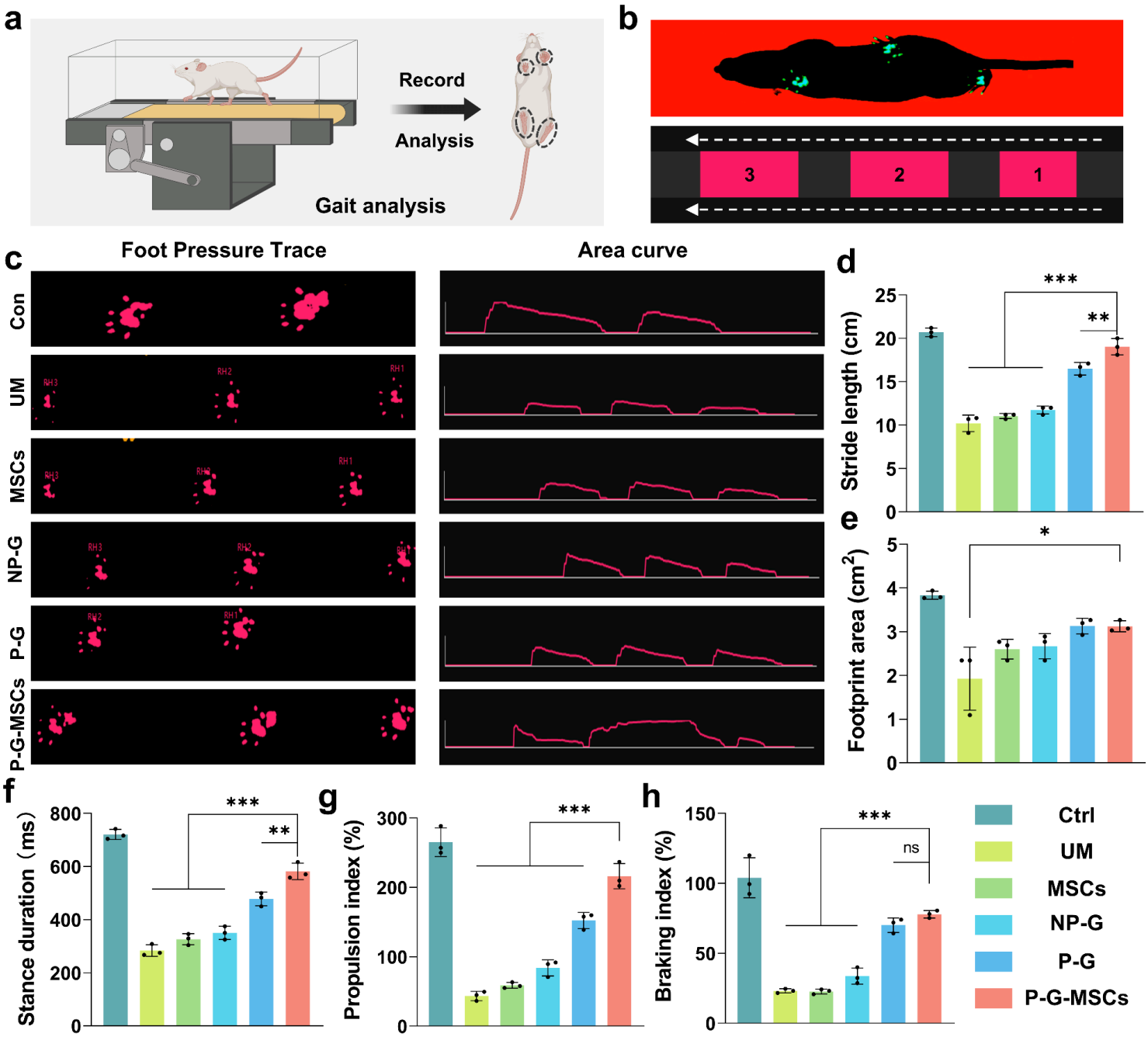


Figure 9

Gait analysis at 8 weeks post-treatment indicates functional recovery after TA VML repair. a) Schematic of gait recording and analysis. b) Illustration of the recording track and analysis zones. c) Representative footprint traces and corresponding contact-area curves for Ctrl, UM, MSCs, NP-G, P-G, and P-G-MSCs groups (operated hind paw). d–h) Quantification of gait parameters including stride length (d), footprint/contact area (e), stance duration (f), propulsion index (g), and braking index (h) of the operated hind paw. Data are presented as mean ± SD (n = 3 biologically independent samples). ***P < 0.001, **P < 0.002, *P < 0.033, ns: no significant difference, one-way ANOVA.

Supplementary Files

This is a list of supplementary files associated with this preprint. Click to download.

- Supportinginformation.docx
- floatimage1.png